

## The oscillating drop technique revisited

This content has been downloaded from IOPscience. Please scroll down to see the full text.

2005 Meas. Sci. Technol. 16 426

(<http://iopscience.iop.org/0957-0233/16/2/013>)

View [the table of contents for this issue](#), or go to the [journal homepage](#) for more

Download details:

IP Address: 134.60.35.121

This content was downloaded on 04/08/2015 at 13:15

Please note that [terms and conditions apply](#).

# The oscillating drop technique revisited

I Egry, H Giffard and S Schneider

German Aerospace Center, DLR, Cologne, Germany

Received 3 June 2004, in final form 9 August 2004

Published 19 January 2005

Online at [stacks.iop.org/MST/16/426](http://stacks.iop.org/MST/16/426)

## Abstract

The oscillating drop technique—in combination with some kind of levitation—is widely used today for the measurement of the surface tension and viscosity of liquids. It is based on Rayleigh's theory for the surface tension driven oscillations of a spherical, force-free, liquid drop.

Unfortunately, this ideal case is never realized in practice. Whereas the influence of the levitation field and finite viscosity on the oscillation frequencies has been discussed by several authors, more practical questions related to the observation of these oscillations have not been addressed before and are the topic of this contribution. In particular, the influence of translational or rotational sample movement, and additional effects due to signal processing are discussed. It is hoped that this paper will help to avoid the many pitfalls inherent in the oscillating drop technique and will thus lead to unambiguous and reliable results.

**Keywords:** oscillating drop technique, levitation, surface tension, viscosity, liquids, Rayleigh theory

## 1. Introduction

The oscillations of a liquid drop have been the subject of numerous theoretical papers. For a non-viscous, force-free, and hence spherical, drop, Rayleigh [1] calculated the oscillation frequencies  $\omega$ ,

$$\omega_l^2 = l(l-1)(l+2) \frac{4\pi}{3} \frac{\gamma}{M} \quad (1)$$

where  $l \geq 2$  is an integer,  $\gamma$  is the surface tension and  $M$  is the mass of the drop. The lowest frequency, corresponding to  $l = 2$ , is called the Rayleigh frequency. This formula provides the basis for the oscillating drop technique. The technical implementation relies on some kind of levitation which provides a freely floating drop, more or less spherical, and an optical detector to record the surface oscillations of the drop. For liquid metals, electromagnetic levitation is the most common technique [2]. This is a containerless, albeit not force-free, method. The levitated sample is subject to both the gravitational force and an electromagnetic levitation force of equal size but opposite direction. These two forces cancel each other only when integrated over the volume of the liquid drop; along the surface of the drop residual forces remain, which lead to its deformation, rendering the assumption of sphericity invalid. The aspherical shape leads to a splitting of

the Rayleigh mode into three frequencies, given by [3]

$$\begin{aligned} \omega_{2,0}^2 &= \omega_R^2 + \omega_t^2 \left( 3.832 - 0.1714 \frac{z_0^2}{R} \right) \\ \omega_{2,\pm 1}^2 &= \omega_R^2 + \omega_t^2 \left( 3.775 + 0.5143 \frac{z_0^2}{R} \right) \\ \omega_{2,\pm 2}^2 &= \omega_R^2 + \omega_t^2 \left( -0.9297 + 2.571 \frac{z_0^2}{R} \right) \end{aligned} \quad (2)$$

with

$$z_0 = \frac{g}{2\omega_t^2} \quad (3)$$

where  $\omega_t^2$  denotes the mean translational squared frequency of the sample,  $g$  is the gravitational acceleration and  $R$  is the radius of the drop. The ideal case of a spherical drop can only be realized approximately in microgravity, where both the residual acceleration and the levitation field are negligibly small.

In addition to translational oscillations, a levitated drop may also perform rotations. If the axis of rotation coincides with the axis of symmetry of the drop, the frequencies of rotating drops are shifted according to Busse [4] by

$$\omega_{l,m}(\Omega) = \omega_{l,m}(0) + \frac{m}{l} \Omega, \quad m \neq 0 \quad (4)$$

where  $\Omega$  is the rotation frequency. Therefore, an oscillating, deformed, rotating drop displays up to  $2l + 1 = 5$  frequencies.

Cummings and Blackburn [3] derived a sum rule for these frequencies, which allows us to determine the surface tension by measuring the frequencies of all five peaks:

$$\frac{1}{5} \sum_n \omega_{2,n}^2 = \frac{32\pi}{3} \frac{\gamma}{M} + 1.9 \overline{\omega_{\text{tr}}}^2 + 0.3 (\overline{\omega_{\text{tr}}}^2)^{-1} (g/R)^2. \quad (5)$$

In summary, the technical realization of the oscillating drop technique leads to a complex frequency spectrum under 1g.

In addition to determining the surface tension, the oscillating drop technique also allows us to measure the viscosity of the liquid through the damping of the oscillations. The damping constant  $\Gamma$ , i.e. the reciprocal decay time to  $1/e$ , is given by [5]

$$\Gamma = \frac{20\pi}{3} \frac{R}{M} \eta \quad (6)$$

where  $\eta$  is the viscosity. For small damping,  $\Gamma \ll \omega$ , the Rayleigh frequency remains unchanged. Unfortunately, this result is valid for force-free drops only, which restricts the applicability of the oscillating drop technique for viscosity measurements to the microgravity environment.

The second component in the experimental set-up is the sensor for surface oscillations. Some groups use a photodetector [6], i.e. a pyrometer, to record the surface oscillations. Such a detector collects the integrated intensity from the incandescent liquid drop. Sample movements cause changes in the effective visible area and lead therefore to an oscillatory component in the detector signal. Other groups use videometry and digital image processing [7]. This yields a two-dimensional time- and space-resolved image of the cross section of the drop, from which the surface oscillations can be reconstructed. In both cases, care has to be taken to relate the obtained signal to the oscillation of the drop radius. Otherwise, artefacts may lead to erroneous results. This will be discussed in detail in the following sections.

## 2. Sample rotation

One of the disturbing effects in determining the surface tension from sample oscillations is the rotation of the sample. Instead of repeating Busse's derivation, we offer a simple and straightforward discussion of the effect of sample rotation, which helps to clarify its role in surface tension measurements.

The radius of a liquid drop, undergoing oscillations with a frequency  $\omega_{l,m}$ , is given by

$$R_{l,m}(t, \vartheta, \varphi) = R_0(1 + \delta(\vartheta) + \varepsilon P_l^m(\vartheta) \cos(m\varphi) \cos(\omega_{l,m}t) e^{-\Gamma_{l,m}t}) \quad (7)$$

where  $R_0$  is the undisturbed static radius of a sphere of equal volume,  $\delta$  is the static deformation,  $\varepsilon$  is the amplitude of the oscillation and  $P_l^m$  is an associated Legendre polynomial. For  $m < 0$ ,  $\cos(m\varphi)$  must be replaced by  $\sin(m\varphi)$ . Equation (7) is the general solution to the problem of an oscillating drop in an external gravitational and levitation field; it represents a normal mode, and general oscillations can be described by linear superpositions of these normal modes. For the following discussion, static deformation  $\delta$  and damping  $\Gamma$  can be safely neglected, and it is sufficient to consider the simpler form

$$\begin{aligned} R_{l,m}^0(t, \vartheta, \varphi) &= R_0(1 + \varepsilon_{l,m}^0(t, \vartheta, \varphi)) \\ \varepsilon_{l,m}^0(t, \vartheta, \varphi) &= \varepsilon P_l^m(\vartheta) \cos(m\varphi) \cos(\omega_{l,m}t). \end{aligned} \quad (8)$$

We can describe a rotating sample in a co-rotating frame of reference, i.e. instead of rotating the sample, we rotate the observer in the opposite direction. Making the crucial assumption that rotation is along the symmetry axis of the problem, we introduce new variables by

$$R' = R, \dots, \vartheta' = \vartheta, \dots, \varphi' = \varphi - \Omega t \quad (9)$$

where  $\Omega$  is the rotation frequency. Substituting into equation (8), we obtain

$$\varepsilon_{l,m}^\Omega(t, \vartheta', \varphi') = \varepsilon P_l^m(\vartheta') \cos(m(\varphi + \Omega t)) \cos(\omega_{l,m}t). \quad (10)$$

Using the addition theorem for the trigonometric functions, we finally obtain

$$\begin{aligned} \varepsilon_{l,m}^\Omega(t, \vartheta', \varphi') &= \frac{\varepsilon P_l^m(\vartheta')}{2} \\ &\times \left[ \cos(m\varphi') \{ \cos((\omega_{l,m} + m\Omega)t) + \cos((\omega_{l,m} - m\Omega)t) \} \right. \\ &\quad \left. + \sin(m\varphi') \{ \sin((\omega_{l,m} + m\Omega)t) - \sin((\omega_{l,m} - m\Omega)t) \} \right]. \end{aligned} \quad (11)$$

This result implies that a drop, oscillating with normal mode  $l, m$  and frequency  $\omega_{l,m}$ , exhibits additional components of the normal mode  $l, -m$  when rotating. Mathematically speaking, this effect stems from the fact that  $\cos(\varphi)$  is not an eigenfunction to the rotation operator  $\partial/\partial\varphi$ . Instead of a single frequency, two frequencies at  $\omega_{l,m} \pm m\Omega$  appear in the oscillation spectrum. This is in contrast to Busse's result: not only is the frequency shifted, but it is split, and two new frequencies appear simultaneously. In addition, the frequency split is twice as large as calculated by Busse for  $l = 2$  (equation (4)). The frequency split is symmetrical. By denoting

$$\omega_{l,m}(\Omega) = \omega_{l,m} + m\Omega \quad (12)$$

we get

$$\omega_{l,|m|} = \frac{1}{2}(\omega_{l,m}(\Omega) + \omega_{l,-m}(\Omega)). \quad (13)$$

In contrast to the sum rule, equation (5), the undisturbed frequency is recovered by linear averaging. If peak splitting due to rotation could be distinguished from splitting due to deformation, the correct procedure would be to first take the linear averages of the  $m = \pm 1$  and  $m = \pm 2$  frequencies and subsequently use the sum rule for the  $m = 0$ ,  $|m| = 1$  and  $|m| = 2$  frequencies.

## 3. Sample translation

In addition to sample rotation, translational oscillations of the sample's centre of mass represent another disturbing effect on the determination of surface oscillations. Depending on the method chosen, the detected signal is related to the radius oscillations in a more or less complicated manner. For example, if the measurement is performed with a pyrometer of a finite measurement spot focused onto the top—the pole—of the sample, the pyrometer signal is proportional to the intensity of radiation collected by the detector, which, in turn, is proportional to the apparent emitting surface and the distance between the detector and sample. If the detector is centred at the edge of the sample—the equator—the signal is proportional to the area covered by the measurement spot. In the first case, the signal is modulated by translational

oscillations along the observation direction, in the second case, it is modulated by translational oscillations perpendicular to the observation direction. The situation is slightly different if the oscillation analysis is performed by image processing. This method allows the elimination of lateral movements by aligning all images with respect to the centre of mass (of the visible cross section). Movements along the observation direction, however, do lead to a modulation, due to a changing magnification factor. This effect can be minimized by using telecentric optics, where the amplification is independent of distance, at least in a certain range.

Restricting ourselves to the case of oscillations along the observation direction, the signal to be analysed will be proportional to

$$S_{l,m}(t) \propto \cos(\omega_{tr}(t + t_0)) \cos(\omega_{l,m}t) \exp(-\Gamma t). \quad (14)$$

Therefore, we expect two frequencies in the spectrum, located at

$$\omega_{l,m}^{\pm}(\omega_{tr}) = \omega_{l,m} \pm \omega_{tr}. \quad (15)$$

#### 4. Data analysis

In real experiments, the ideal oscillation signal is blurred mainly by two effects: (i) noise generated by the electronic and optical components and (ii) modulation due to sample movement and variations in the optical path. It is the aim of this section to define an optimal method for extracting the desired information from such signals, in particular with respect to the determination of the damping constant  $\Gamma$ . To this end, numerical tests were performed using synthetic test functions. In a second step, the method was applied to data recently obtained during a parabolic flight of the TEMPUS electromagnetic levitation facility [8].

##### 4.1. Numerical tests without noise

In order to choose the most accurate of various possible methods of determining the damping constant of an oscillating signal, a test function was constructed, the methods applied and the results compared to the expected value.

The function investigated was

$$S(t) = \cos(2\pi\nu_1 t + \varphi) \cos(2\pi\nu_2 t) \exp(-\Gamma t) \quad (16)$$

with  $\nu_1 = 4$  Hz,  $\nu_2 = 43$  Hz,  $\varphi = \pi/12$ ,  $\Gamma = 1/5$ . ( $\nu_2$  was intentionally chosen so as not to be a multiple of  $\nu_1$ .)

Two possible methods to calculate the damping constant were considered. The first requires the measurement of the half-width of a peak in the Fourier transform of the signal. The second method uses a plot of the natural logarithm of the square of the function. In both cases the Origin<sup>®</sup> software package [9] was used.

Both methods were applied to  $S(t)$  over various periods  $T$  and with varying sample point densities  $dt$ .  $T$  is equal to the point density times the number of points used  $N$ :  $T = N dt$ . Each method was applied to data with  $dt = 1/50, 1/100, 1/200$  and  $1/500$ . For each  $dt$ , the number of points was varied, letting  $N = 256, 512, 1024, 2048$  and  $4096$ .

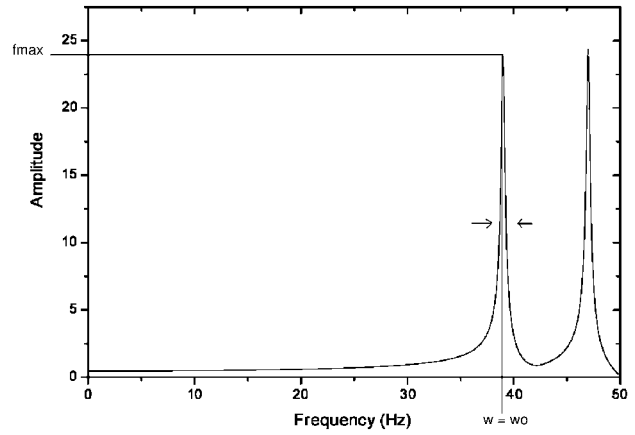


**Figure 1.** Fourier transform of  $S(t)$ : height and peak width can be easily determined graphically.

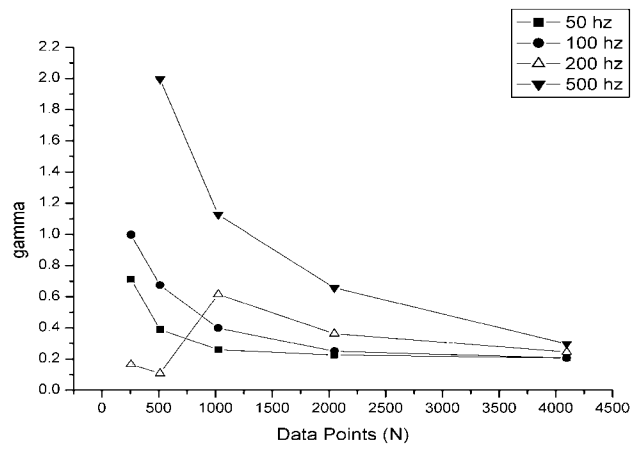


**Figure 2.** Convergence of  $\Gamma$  with increasing  $N$  using the half-width method.

**4.1.1. Half-width method.** The derivation of the damping constant from the peak width follows from the definition of the Fourier transform. We used Origin's graph of  $r(\nu) = \sqrt{\text{Re}^2 + \text{Im}^2}$  rather than the graph of the real part alone. For  $r(\nu)$ , the half-width  $\Delta\nu_{1/2}$  is related to the damping constant via

$$\Delta\nu_{1/2} = \frac{\sqrt{3}}{\pi} \Gamma. \quad (17)$$

The Fourier transform of  $S(t)$  is shown in figure 1. Due to the modulation, two peaks are visible at  $\nu_2 \pm \nu_1$ , according to equation (15). Peak height and peak width can be determined easily.

The first results, with few data points, were very inaccurate. At higher frequencies, the total time reflected in a given  $N$  points was increasingly shorter, thus less damping occurs and the determined constant is less accurate. As  $N$  increases, however, the calculated values converge to the known value. The results are plotted in figure 2.

**4.1.2. Logarithmic method.** The second method investigated required taking the natural logarithm of the square of the original function. A fit over the maxima produces a line with a slope of  $-2\Gamma$ :

$$\ln(S(t)^2) = \ln(\cos^2(2\pi\nu_1 t + \varphi) \cos^2(2\pi\nu_2 t)) - 2\Gamma t. \quad (18)$$

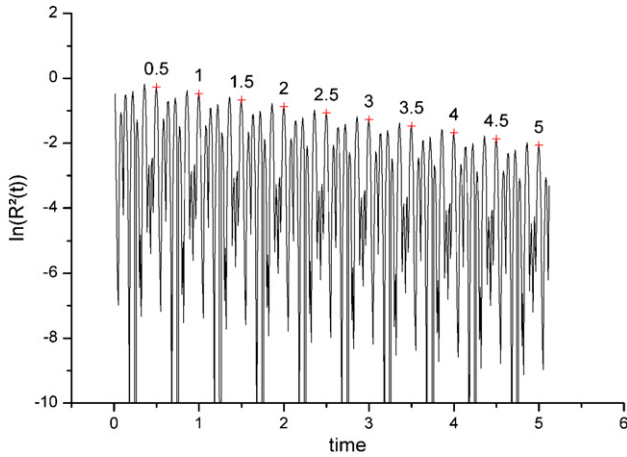


**Figure 3.** Natural logarithm of the squared function with peaks indicated.

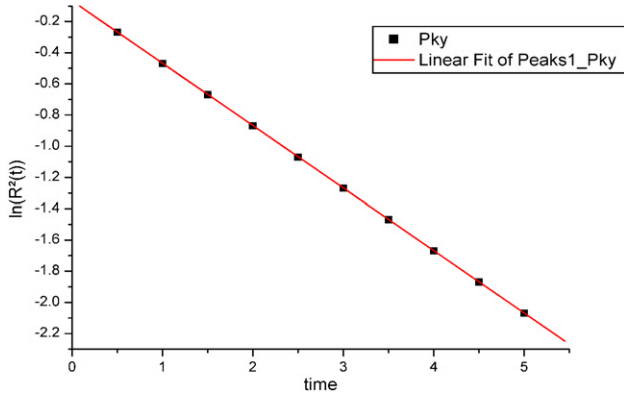


**Figure 4.** The peaks plotted and fitted linearly.

To select the maxima of this function, the Origin tool ‘Pick Peaks’ was used. This tool uses a square box to find the local maxima. Therefore, the selection of points is influenced by the width and height settings entered for the search rectangle. The height and width values were adjusted until sufficient maxima were selected, as shown in figure 3.

This method was consistently accurate and easy to evaluate. The positions of the maxima could be well fitted linearly, in accordance with equation (18), as shown in figure 4. Figure 5 summarizes the results. It can be seen that with increasing  $N$ , the values converge towards 0.2, even faster than with the half-width method.

#### 4.2. Added random noise

The next step was to determine if the above methods worked on a signal with 10% random noise added. Consequently, after the function is damped below a value of 0.05, the noise overwhelms the function. This is seen clearly in figure 6, where the decreasing line of the maxima levels off abruptly. The FFT of the noisy signal is shown in figure 7. The values of  $\Gamma$  found by measuring the peak width of the noisy signal are shown in figure 8. Despite the noise, the values converge to the correct result.

On the other hand, the logarithmic method does not work well for noisy signals, due to the levelling off, as shown in

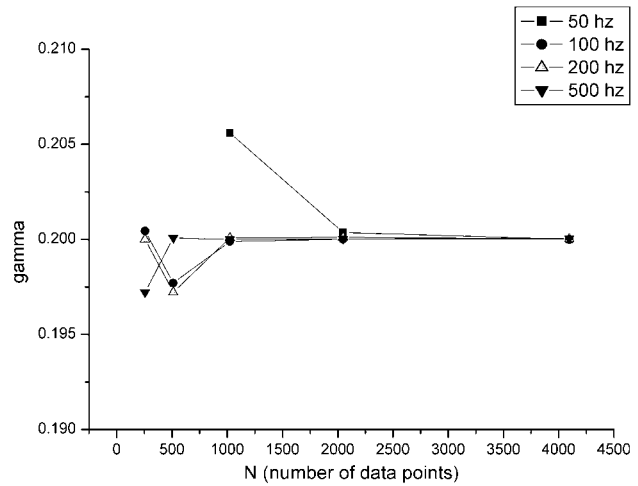


**Figure 5.** Convergence of  $\Gamma$  with increasing  $N$  using the logarithmic method.

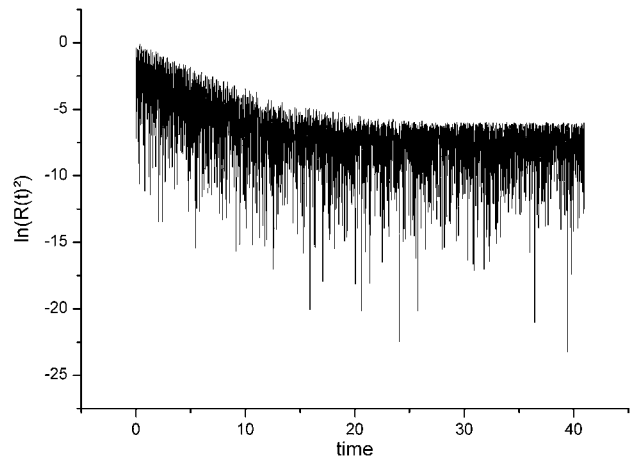


**Figure 6.** A plot of  $\ln(S(t)^2)$  with noise added.

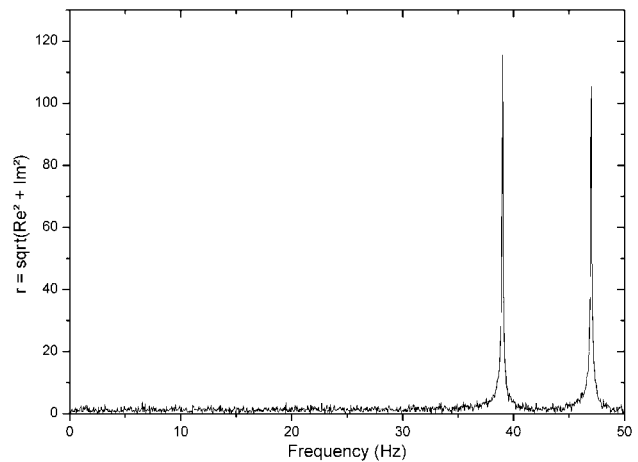


**Figure 7.** FFT of the noisy signal.

figure 6. As can be seen from figure 9, the results were irregular, suggesting that this method is much less accurate with a noisy signal.

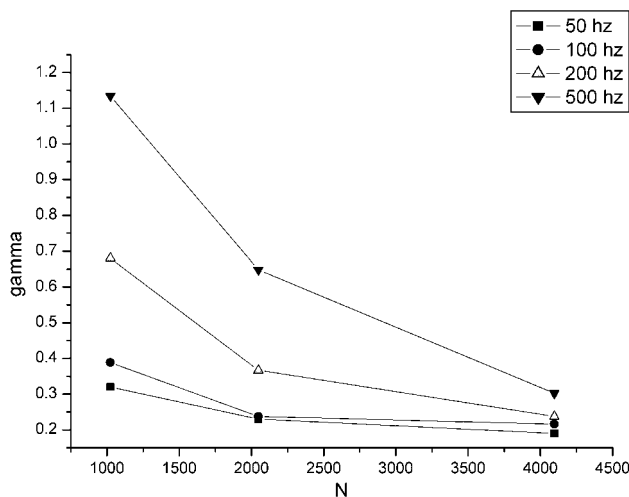


Figure 8. Gamma values determined from peak half-width.

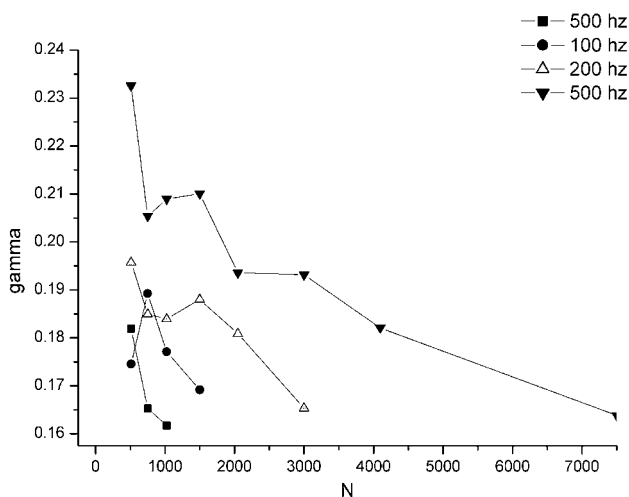


Figure 9. Results determined using the logarithmic method.

#### 4.3. Application: CuCo levitation data

The methods described above were applied to data from parabolic flight experiments on a Cu–Co sample [8]. During one experiment, a  $\text{Cu}_{38}\text{Co}_{62}$  sample was pre-heated during the 2g-phase, levitated, melted and cooled during the 20 s of the microgravity phase. During cooling, three pulses were applied to trigger surface oscillations at three different temperatures. From the video data, the radius of the sample was determined as a function of time as shown in figure 10. The sample was subjected to three pulses, each of which followed an exponential damping. Each pulse was analysed separately.

From the damping constant calculated from each pulse, the viscosity of the metal was obtained. The temperature is slightly lower for each successive pulse, while it remains fairly constant within each pulse. The viscosity is found using equation (6). The Cu–Co sample weighed 0.8 g and had an initial radius of 2.75 mm. The results are listed in table 1. The viscosities thus determined are in the expected range for liquid metals. Within the error bars, both methods yield identical results. Also, the temperature dependence of the viscosity is correct, showing an increase with decreasing temperature.

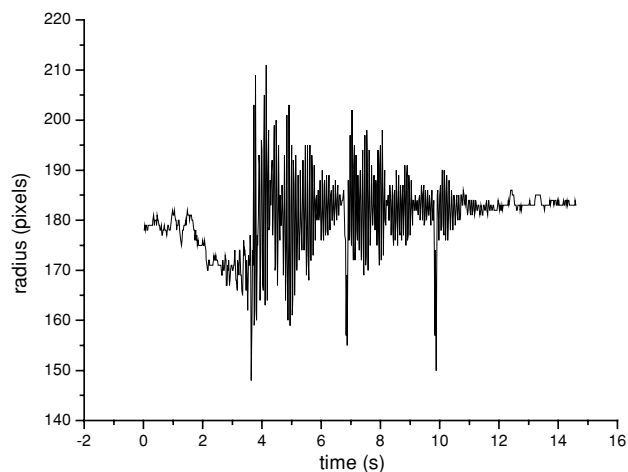


Figure 10. Plot of the raw data from the video camera taken at 50 Hz.

Table 1. Calculated values of the viscosity of CuCo at various temperatures.

Method	Pulse	Gamma ( $\text{s}^{-1}$ )	Viscosity (mPa s)
Peak width	Heating coil off	0.776 97	10.858
Natural log	Heating coil off	0.639 54	8.938
Natural log	Pulse 1	0.529 68	7.402
Natural log	Pulse 2	1.039 15	14.522

Table 2. Calculated surface tension for CuCo. The average of the five highest peaks was used to calculate the frequency,  $\nu$ .

Pulses	Frequency	Surface tension ( $\text{N m}^{-1}$ )
Total signal	36.49	1.26
Heating coil off	36.47	1.26
1	36.52	1.26
1 (ave of squares)	36.55	1.27
2	36.91	1.29
2 (ave of squares)	36.86	1.29
Total signal (highest peak only)	35.94	1.22

Finally, also the surface tension of the samples was calculated by applying equation (2). The drop's five oscillation modes produce five peaks in the Fourier transformed signal (for  $m = 0, \pm 1, \pm 2$ ). The average of the five highest peaks was used for the calculation of the surface tension. For each spectrum, both the linear average and squared average were evaluated and are listed in table 2. From the experiment protocol, a temperature can be assigned to each instant in time, and in particular to the three trigger pulses. Therefore, the temperature dependence of the surface tension could be derived. This is shown in figure 11. The values thus obtained are in reasonable agreement with published values for Cu–Co [10]. In conclusion, both signal processing methods produced reasonable results. Except for the second pulse, which had limited data, the values calculated for the viscosity were close to those expected (between 3 and 6 mPa s). Despite having a noisy signal, the logarithmic method worked well. It was impossible to apply the half-width method to each pulse because the cluster of five peaks on the Fourier transform makes the half-height value difficult to determine.



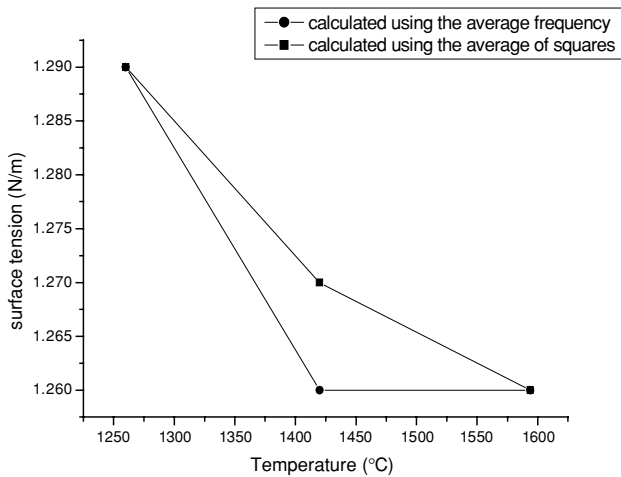


Figure 11. Surface tension as a function of temperature.

accurately. Dividing the peaks on such a spectrum is possible, but time-consuming. Using the average frequency of the peaks, however, was sufficient in the case of calculating the surface tension. As expected, the surface tension increased with decreasing temperature.

## 5. Conclusions

Whereas external fields lead to a splitting and shifting of the oscillation frequency of a liquid drop, sample rotations and sample translation induce a modulation of the signal and create sidebands. The latter two effects can be eliminated by a linear average of the obtained frequency, while the magnetic field effect can be accounted for by a quadratic sum rule. If all effects are present simultaneously, as is usually the case, the most accurate evaluation of the frequency spectrum consists of the following steps:

- Identification of the oscillation modes through image processing.
- Linear averaging of frequencies with equal  $|m|$ .
- Application of equation (2) to the remaining three frequencies with known  $|m|$ .

As shown in figure 11, the application of the quadratic sum rule, equation (5), may lead to a small difference in the result, which has to be accepted, if the above procedure is not possible. Concerning the determination of the viscosity from

the oscillation spectrum, the influence of the magnetic field is known to be strong [11], but there is no satisfactory theory [12] to take this effect into account. Consequently, viscosity measurements are restricted to microgravity conditions.

The determination of the damping constant from the signal is complicated by two factors: beat effects due to modulation and noise. Two methods have been proposed to determine the damping constant, one working in the frequency domain, based on the evaluation of the half-width of the peaks, the other working in the time domain, determining the slope of the logarithm of the squared signal. For small noise, the latter is superior, but it is more sensitive to the noise level. In the practical application discussed above, both methods yield similar results.

## References

- [1] Lord Rayleigh 1879 Capillary phenomena of jets *Proc. R. Soc.* **29** 71–97
- [2] Herlach D M, Cochrane R F, Egry I, Fecht H J and Greer A L 1993 Containerless processing in the study of metallic melts and their solidification *Int. Mater. Rev.* **38** 273–347
- [3] Cummings D L and Blackburn D A 1991 Oscillations of magnetically levitated aspherical droplets *J. Fluid Mech.* **224** 395–416
- [4] Busse F H 1984 Oscillations of a rotating liquid drop *J. Fluid Mech.* **142** 1–8
- [5] Chandrasekhar S 1959 The oscillations of a viscous liquid globe *Proc. Lond. Math. Soc.* **9** 141–9
- [6] Brooks R F and Mills K C 1993 Measurement of the thermophysical properties of melts by a levitated-drop method *High Temp.—High Pressures* **25** 657–64
- [7] Sauerland S, Eckler K and Egry I 1992 High precision surface tension measurements on levitated aspherical liquid nickel droplets by digital image processing *J. Mater. Sci. Lett.* **11** 330–3
- [8] Kolbe M, Reutzel S, Patty A, Egry I, Ratke L and Herlach D M 2004 Undercooling and demixing of Cu–Co melts in the TEMPUS facility during parabolic flight *Multiphase Phenomena and CFD Modeling and Simulation in Materials Processes* ed L Nastac and B Q Li (Warrendale, PA: TMS) pp 55–63
- [9] Origin® 2002 Originlab Corporation Northampton, MA, USA
- [10] Eichel R A and Egry I 1999 Surface tension and surface segregation of liquid cobalt–iron and cobalt–copper alloys *Z. Metallk.* **90** 371–5
- [11] Schneider S 2002 Viskositäten unterkühlter Metallschmelzen *PhD Thesis RWTH Aachen*
- [12] Bratz A and Egry I 1995 Surface oscillations of electromagnetically levitated viscous metal droplets *J. Fluid Mech.* **298** 341–59